40. R. Gersonde *et al.*, *Paleoceanography* **18**, 1061 (2003); 10.1029/2002PA000809.
41. R. Gersonde, X. Crosta, A. Abelmann, L. Armand, *Quat. Sci. Rev.* **24**, 869 (2005).
42. R. Gersonde, U. Zielinski, *Palaeogeogr. Palaeoclimatol. Palaeoecol.* **162**, 263 (2000).
43. S. R. Hemming, *Rev. Geophys.* **42**, RG1005 (2004); 10.1029/2003RG000128.
44. J. F. McManus, R. Francois, J. M. Gherardi, L. D. Keigwin, S. Brown-Leger, *Nature* **428**, 834 (2004).
45. H. C. Bostock, B. N. Opdyke, M. K. Gagan, L. K. Fifield, *Paleoceanography* **19**, PA4013 (2004).
46. K. Pahnke, R. Zahn, *Science* **307**, 1741 (2005).
47. P. M. Grootes, M. Stuiver, J. W. C. White, S. Johnsen, J. Jouzel, *Nature* **366**, 552 (1993).
48. A. M. Piotrowski, S. L. Goldstein, S. R. Hemming, R. G. Fairbanks, *Earth Planet. Sci. Lett.* **225**, 205 (2004).
49. Two samples at 15.0 ka (1180 m) and 14.3 ka (1221 m), both from Gregg Seamount, have Δ^{14}C values ~25‰ and ~0‰ below the atmosphere, respectively. From the end of Heinrich 1 to ~14.2 ka, the atmospheric radiocarbon content dropped at least as fast as the decay rate, leading to a situation in which the decrease in the radiocarbon content of the atmosphere could "overtake" the decay rate in an isolated water mass. Two samples from the end of the Younger Dryas are also within error of the atmospheric value and lie at the end of a marked drop in the atmospheric radiocarbon content (28).
50. L. C. Skinner, N. J. Shackleton, *Paleoceanography* **19**, PA2005 (2004); 10.1029/2003PA000983.
51. This trend is well constrained by five BF-PF pairs, three of which (including the oldest and youngest) are from the same core.
52. K. A. Hughen *et al.*, *Nature* **391**, 65 (1998).
53. R. G. Fairbanks *et al.*, *Quat. Sci. Rev.* **24**, 1781 (2005).
54. Y. J. Wang *et al.*, *Science* **294**, 2345 (2001).
55. We acknowledge the Comer Foundation for Abrupt Climate Change, the Henry Luce Foundation, the American Chemical Society Petroleum Research Fund, and NSF grant numbers OCE-0096373 and OCE-0095331. We also thank all members of the cruise AT7-35 to the New England Seamounts.

REPORTS

Postseismic Mantle Relaxation in the Central Nevada Seismic Belt

Noel Gourmelen* and Falk Amelung

Holocene acceleration of deformation and postseismic relaxation are two hypotheses to explain the present-day deformation in the Central Nevada Seismic Belt (CNSB). Discriminating between these two mechanisms is critical for understanding the dynamics and seismic potential of the Basin and Range province. Interferometric synthetic aperture radar detected a broad area of uplift (2 to 3 millimeters per year) that can be explained by postseismic mantle relaxation after a sequence of large crustal earthquakes from 1915 to 1954. The results lead to a broad agreement between geologic and geodetic strain indicators and support a model of a rigid Basin and Range between the CNSB and the Wasatch fault.

Some of the largest earthquakes in North America during the 20th century were located in the Central Nevada Seismic Belt (CNSB), one of the known actively deforming areas in the Basin and Range (Fig. 1). The 1915 Pleasant Valley earthquake [seismic magnitude (M_s) 7.2 to 7.6], the 1932 Cedar Mountain earthquake (M_s 7.2), and the 1954 Rainbow Mountain–Fairview Peak–Dixie Valley earthquake sequence (four events, M_s 6.8 to 7.2, in a 6-month period) were right lateral to normal slip events, and ruptured a noncontinuous stretch of north-northeast striking range front faults ~250 km in length.

The present-day deformation across the CNSB is puzzling for two reasons: (i) The deformation rate during Holocene time is believed to be 0.5 to 1.3 mm/year (*1–4*), which is lower than the 2 to 4 mm/year measured by Global Positioning System (GPS) data (*5–7*); and (ii) GPS measurements reveal a zone of east-west contraction east of the CNSB (*5–9*) that is difficult to reconcile with current geodynamic models of the region, which involve east-west extension and right-lateral shear. One possible explanation for these two discrepancies is that the GPS data record not only the long-term deformation, but also transient deformation associated with viscous or viscoelastic relaxation of the lower crust or upper mantle after the last century's earthquakes (*7*, *8*, *10*). We used 8 years of interferometric synthetic aperture radar (InSAR) data to investigate ongoing deformation in the CNSB.

The SAR imagery covers a swath nearly 700 km long (seven conventional SAR frames) acquired by the European Remote Sensing Satellites ERS-1 and ERS-2 between 1992 and 2000 to investigate crustal deformation at the CNSB (*11*). InSAR measures changes in the radar line-of-sight (LOS) distance between the satellite and the surface of Earth; it is most sensitive to vertical movement and somewhat sensitive to east-west movements (*12*). A ground velocity map in LOS direction is shown in Fig. 1. The map was obtained by averaging (stacking) eight independent long-term interferograms, each spanning 4 to 7 years (Table 1). Most of the interferograms have perpendicular baselines smaller than 100 m. We used these pairs because larger baselines lead to decorrelation of the interferometric phase. We obtained the velocity map by dividing the cumulative LOS displacement of the interferograms by the cumulative interferogram period of 37 years. We assumed that uncertainties associated with the satellite orbits cause linear phase ramps across the interferogram and removed any linear trend from the data.

The resulting ground velocity map shows a bulge with LOS velocity as high as ~3 mm/year of relative motion with respect to the margin of the interferograms, centered in the epicentral area of the 1915 Pleasant Valley and 1954 Dixie Valley earthquakes. About 1 to 2 mm/year is detected in the areas of the Fairview Peak and Cedar Mountain earthquakes. The map also shows an area of subsidence in the northern part of the interferogram in the area of the Lone Tree gold mine, presumably caused by groundwater pumping in support of open-pit mining operations.

To test whether the observed phase signature is real deformation or a processing artifact, we generated another stack using eight interferograms covering shorter time periods (each <4 months, total time span ~2 years). Because no deformation is expected from such a stack, a residual signal would reveal processing, atmospheric, or orbital artifacts. To obtain comparable LOS velocities, we divided the cumulative LOS displacement of the short-term stack by the cumulative time of the long-term stack (37 years). The averaged LOS velocities based on the long-term stack (Fig. 2) show a long-wavelength signal of ~3 mm/year of LOS velocity, but the short-term stack does not show this signal. This result indicates that the

Division of Marine Geology and Geophysics, Rosenstiel School of Marine and Atmospheric Sciences, University of Miami, Miami, FL 33149, USA.

*To whom correspondence should be addressed. E-mail: ngourmelen@rsmas.miami.edu

Fig. 1. 1992–2000 LOS velocity map for the area of the 1915–1954 Nevada earthquakes together with epicenters (blank circles), focal mechanisms (spheres), and surface ruptures. Green arrows, campaign GPS velocities (7); red arrows, Basin and Range Geodetic Network (BARGEN) permanent GPS velocities and site names (9). LOS is velocity considered positive for decreasing distance between ground and satellite.
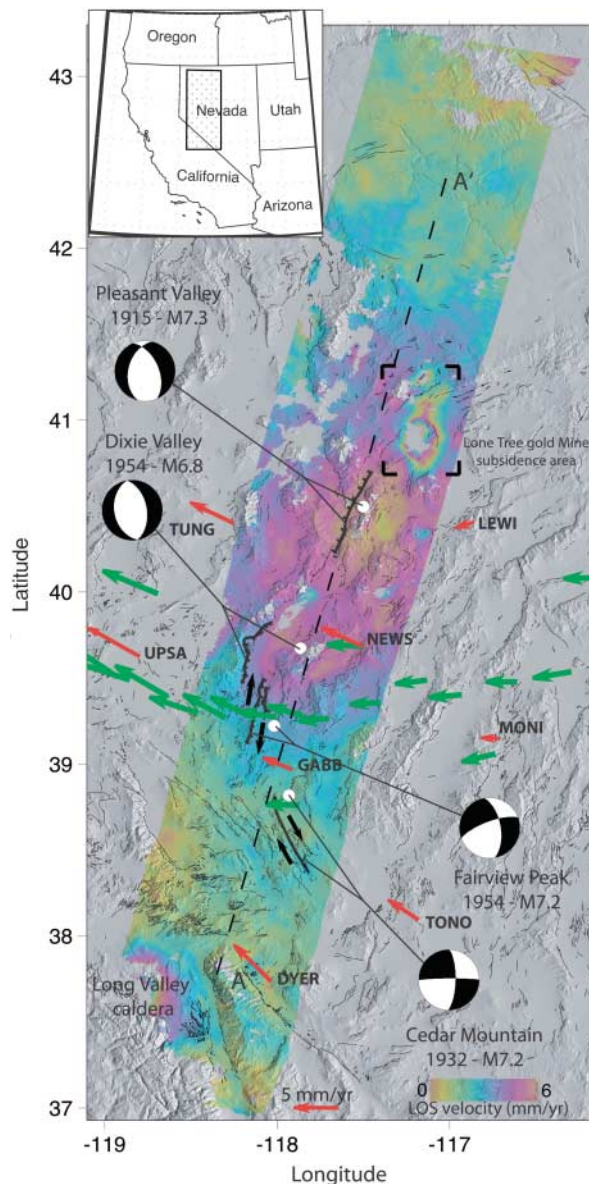

Table 1. Dates of SAR acquisitions used for interferometry and perpendicular baselines.

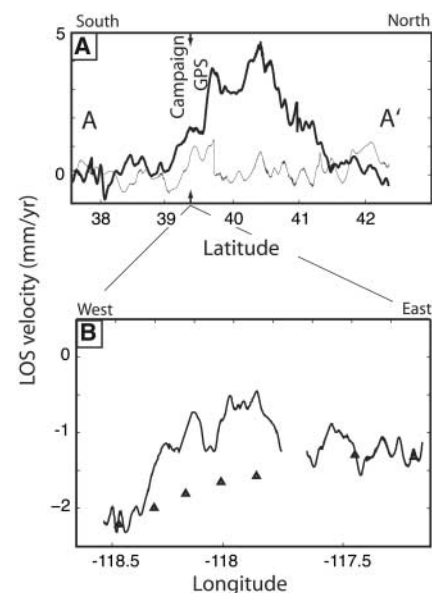| Date range	Perpendicular baseline (m)
25 July 1992– 21 September 1999	3
1 May 1993– 10 November 1998	−41
18 September 1993– 6 October 1998	−18
16 October 1995– 23 February 1999	72
17 October 1995– 23 May 2000	−101
21 November 1995– 1 August 2000	180
9 April 1996– 5 September 2000	−71
14 May 1996– 19 May 1998	84

Fig. 2. (A) LOS velocity relative to the margins of the interferogram along a north-south profile obtained from long-term (thick line) and short-term (thin line) interferograms; the location of the GPS profile is shown by arrows. (B) LOS velocity relative to stable North America along a roughly east-west profile coinciding with the GPS campaign sites (line), together with LOS component of horizontal GPS velocities (triangles). The uncertainty on the LOS component of horizontal GPS velocities is on average 0.4 mm/year.

observed phase signature represents real ground deformation. Both profiles show a short-wavelength variation of 1 to 2 mm/year LOS velocity attributable to the atmospheric variability.

To test whether the InSAR data can be explained by horizontal deformation as measured by campaign GPS measurements, we compared the LOS component of the horizontal GPS with the InSAR data. The GPS data (7) show a roughly linear increase of ~3 mm/year in velocity magnitude westward across the interferogram. This corresponds to a decrease in LOS velocity of 0.8 mm/year (Fig. 2B) (13). Transferring the InSAR data into the GPS reference frame shows that the InSAR data cannot be explained by horizontal motion (Fig. 2B). The best explanation for the bulge in the InSAR data (2 mm/year at this latitude) is therefore local uplift. Analysis of the vertical velocities of the

permanent GPS network indicates that the station NEWS, situated in the area of maximum LOS velocity, is moving upward with respect to the surrounding stations (14), in agreement with the InSAR map.

One assumption is that errors associated with satellite orbit result in linear phase ramps in the interferograms. It is also well known that orbital errors may introduce more complex large wavelength errors. We are confident, however, that the observed signal represents real deformation because LOS velocity maps based on the same SAR acquisitions but different interferograms showed similar results, because the velocity map based on short-term interferograms does not show any similar signature even though they are based on the same acquisitions, and because the detected deformation has a maximum velocity in the area of the largest historic earthquake, which is geologically plausible and consistent with GPS

measurements. We attempted to verify the result with the use of data from the adjacent swath to the east, but we could not produce an interferogram with a similar cumulative time.

We tested whether the observed deformation may be caused by postseismic relaxation of Earth's crust and mantle after the 1915 to 1954 earthquakes. We assumed linear viscoelastic rheology and considered two- and three-layer Earth models using the methodol-

Table 2. Earthquake parameters used in the modeling. The magnitude values are obtained by inversion of the InSAR data and the postseismic models. See text for references.

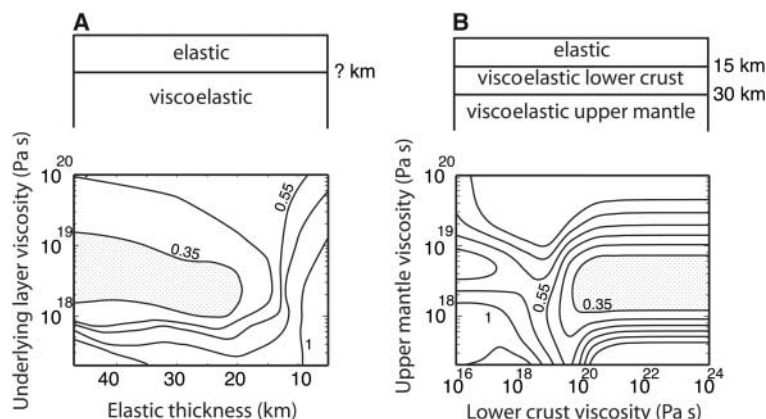| Location and date	Latitude	Longitude	Length (km)	Depth (km)	Strike	Dip	Rake	Magnitude	
								Published (M_s)	Inversion (M_w)
Pleasant Valley (3 October 1915)	40.5	−117.5	59	9	194°	44°	−61°	7.6	7.3
Cedar Mountain (21 December 1932)	38.80	−117.98	70	13	350°	72°	−179°	7.2	7.1
Fairview Peak (16 December 1954)	39.20	−118.00	40	15	004°	60°	−150°	7.2	7.2
Dixie Valley (16 December 1954)	39.67	−117.87	42	12	008°	30°	−90°	6.8	6.7

Fig. 3. Misfit between observed and modeled deformation. (**A**) Two-layer Earth model consisting of an elastic plate overlying a viscoelastic half-space. (**B**) Three-layer Earth model consisting of an elastic and a viscoelastic layer over a viscoelastic half-space.

Fig. 4. (**A**) Data and best fitting postseismic relaxation model (Lone Tree gold mine deformation area has been masked out). (**B**) Profile [dashed lines in (A)].

ogy of (*15*). The sources for postseismic deformation were four earthquakes: the 1915 Pleasant Valley, 1932 Cedar Mountain, and 1954 Fairview Peak and Dixie Valley earthquakes. We did not include the main 1954 Rainbow Mountain earthquake (*16*). We used fault parameters in the range of values published after field measurements (*17*, *18*), geodetic modeling (*19*), and seismologic modeling (*20–22*) (Table 2). For the Dixie Valley fault we used a dip of 30° (*23*) because the maximum LOS velocity >15 km east of the surface trace of the fault suggested a low-angle dipping fault. We also inverted for the magnitudes of the earthquakes, allowing a deviation of 0.3 from the magnitudes (*21*, *22*) and from 7.1 to 7.7 for the Pleasant Valley earthquake.

Our data set consists of 11,072 equally spaced (~1.7 km spacing) LOS velocity measurements. Best fitting models are characterized by a minimum of the difference between the data and the model predictions (*24*). We varied the grid spacing and used quadtree decompositions of the data to test whether the modeling results are sensitive to the sampling method, and we found that this is not the case.

We first used a two-layer Earth model consisting of an elastic plate overlying a viscoelastic half-space to obtain an estimate of the elastic thickness of the crust and of the viscosity of the underlying substrate. We conducted a grid search varying the elastic thickness and the viscosity. For each grid point we conducted a linear inversion for the slip magnitude to account for the uncertainty of the earthquake magnitude. The lowest misfits (0.3 mm/year) were found for models with an elastic thickness larger than 20 km and a subcrustal viscosity of 10^{18} to 10^{19} Pa·s (Fig. 3).

We also used a three-layer Earth model consisting of an elastic layer overlying two viscoelastic layers, representing the elastic upper crust, the viscoelastic lower crust, and the viscoelastic upper mantle. We used an elastic layer thickness of 15 km (seismogenic thickness) and a lower crust thickness of 15 km so that the crustal thickness agreed with the 30 km inferred from seismic reflection data (*25*). We varied the viscosity of the lower crust and of the uppermost mantle. For this model the lowest misfits were found for lower crustal viscosities larger than 10^{20} Pa·s and for upper-mantle viscosities of 1×10^{18} to 7×10^{18} Pa·s. The LOS velocity predicted by the best fitting model explains the large wavelength deformation (Fig. 4). We consider models with normalized root mean square (NRMS) < 0.35 mm/year as reasonable models.

The InSAR data cannot be explained with postseismic models if we use the published earthquake magnitudes, and therefore we inverted for the magnitudes. This is desirable because the magnitudes are not well constrained by the instrumental data. In fact, our study shows that precise postseismic deformation data can be used to estimate the magnitude of historic earthquakes as long as an estimate of the focal mechanism is available.
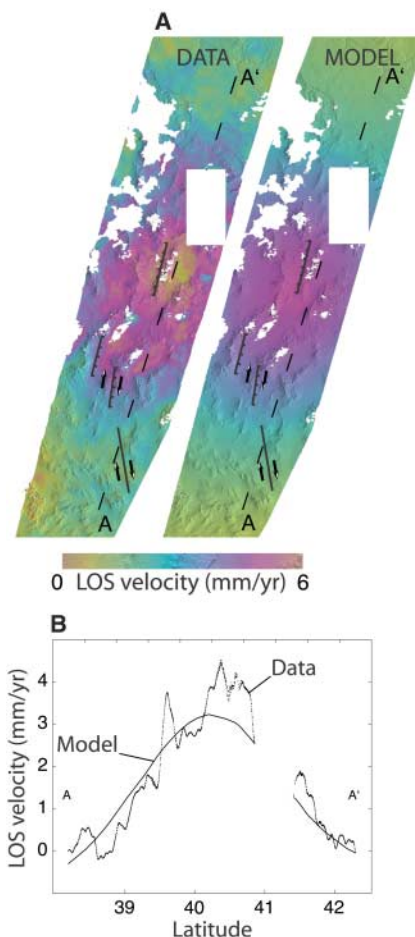
We found the same magnitudes for the two- and three-layer models (Table 2). The magnitude of the Fairview peak earthquake remains unchanged at moment magnitude (M_w) 7.2. For the Cedar Mountain and Dixie Valley earthquakes, we find values of M_w 7.1 and M_w 6.7, corresponding to a reduction of 10% from the published magnitudes. For the Pleasant Valley earthquake we find M_w 7.3, smaller than the seismologic estimates of 7.6 (*26*) but in agreement with the value of 7.2 derived from surface faulting (*17*). The cumulative M_w of the four modeled earthquakes is 7.55.

It is noteworthy that the area of deformation is larger than the epicentral area of the earth-

Fig. 5. Bottom: Magnitude of horizontal campaign GPS velocities along an east-west profile through the Basin and Range (7). Upper line, measured velocities; lower line, measured velocities minus model-predicted postseismic deformation. Top: Simplified tectonic map of the Basin and Range. Triangles, locations of GPS stations; CNSB, Central Nevada Seismic Belt; WL, Walker Lane.
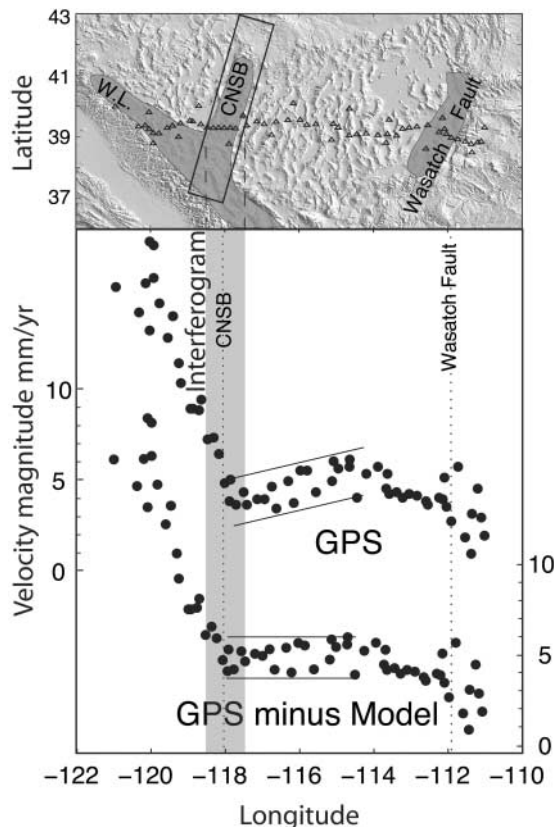
quakes and that the deformation field lacks short-wavelength features. The lithospheric rheology acts as a low-pass filter that translates the instantaneous short-wavelength earthquake stress into long-wavelength deformation lasting several decades. This suggests that the upper parts of the lithosphere behave elastically on the time scale of our data and that viscous relaxation occurs only at greater depth. For the two-layer model we find a lower bound for the thickness of the elastic layer of 20 km and a viscosity of the underlying substrate of 10^{18} to 10^{19} Pa·s. Using a three-layer model, we find a viscosity of the substrate in the same range and a viscosity of the intermediate layer (lower crust) larger than 10^{20} Pa·s. These results suggest that most of the crust or the entire crust of the Basin and Range lithosphere (including the lower crust) behaved elastically for at least 80 years after these large earthquakes. Relaxation of the earthquake-induced stress occurred by viscous flow in the mantle. These rheology estimates are consistent with previous studies in the Basin and Range and in the Mojave Desert, which also showed an elastic or high-viscosity lower crust and a low-viscosity upper mantle (27–31).

The GPS data collected along an east-west profile indicate an area of low-rate contraction east of the CNSB (Fig. 5, 7). A profile of secular ground velocity, obtained by removing the model-predicted postseismic velocities from the GPS vectors (32), does not show this

contraction but shows only deformation west of the CNSB (Fig. 5). This suggests that the GPS-measured contraction is a postseismic effect and supports the simple geodynamic picture for the Basin and Range in which the central Basin and Range is an essentially undeforming block with deforming boundary zones (i.e., the CNSB and the Walker Lane to the east and the Wasatch fault zone to the west) (5, 33, 34). This interpretation is consistent with the geodetic microplate model for the Central Basin and Range of (9). The residual velocity across the CNSB itself is 0 to 2 mm/year, in agreement with geologic estimates of deformation (4). This implies that the CNSB does not have the elevated seismic potential attributed on the basis of the GPS measurements (35).

References and Notes
1. The variability of rate estimation from paleoseismologic study depends on the method used to measure the net slip vector (2–4). At the latitude of the GPS profile (at ~39.3°N), we refer to the CNSB as the area including the Rainbow Mountain, Fourmile Flat, Fairview Peak, and Sand Springs faults (4). This corresponds to the area between −118.646° and −117.712° between the GPS sites B220 and C200 of (7).
2. J. W. Bell et al., Geol. Soc. Am. Bull. **111**, 791 (1999).
3. S. J. Caskey, J. W. Bell, A. R. Ramelli, S. G. Wesnousky, Bull. Seismol. Soc. Am. **94**, 1255 (2004).
4. S. J. Caskey, J. W. Bell, A. Ramelli, L. Guerrieri, Bull. Seismol. Soc. Am. **94**, 1229 (2004).
5. W. Thatcher et al., Science **283**, 1714 (1999).
6. J. L. Svarc, J. C. Savage, W. H. Prescott, A. R. Ramelli, J. Geophys. Res. **107**, 10.1029/2001JB000579 (2002).
7. W. C. Hammond, W. Thatcher, J. Geophys. Res. **109**, 10.1029/2003JB002746 (2004).
8. B. Wernicke, A. M. Friedrich, N. A. Niemi, R. A. Bennett, J. L. Davis, GSA Today **10**, 1 (November 2000).
9. R. Bennett, B. P. Wernicke, N. A. Niemi, A. M. Friedrich, J. L. Davis, Tectonics **22**, 10.1029/2001TC001355 (2003).
10. E. A. Hetland, B. H. Hager, J. Geophys. Res. **108**, 10.1029/2002JB002257 (2003).
11. For SAR processing we used the commercial FOCUS processor, and for InSAR processing we used ROI_PAC v2.2.1 software (Jet Propulsion Laboratory). We did not reestimate the baseline between the satellite orbits with the use of topographic information because this may introduce second-order phase ramps. For InSAR studies over the Basin and Range, see (36).
12. The unit vector from the ground toward the radar is (0.384, −0.075, 0.92) in an [east, north, up] coordinate system for descending orbit.
13. LOS velocity is with respect to stable North America using the reference frame realization of (7).
14. G. Sella, personal communication.
15. F. F. Pollitz, J. Geophys. Res. **102**, 17921 (1992).
16. The Rainbow Mountain earthquake was M_w 6.8 to 7 (3, 21), predominantly a strike-slip earthquake. Modeling this earthquake showed that the postseismic deformation in LOS direction is more than an order of magnitude smaller than for the Dixie Valley earthquake, and thus it can be safely neglected.
17. R. E. Wallace, U. S. Geol. Surv. Prof. Pap. 1274-A (1984).
18. J. Caskey, S. G. Wesnousky, P. Zhang, D. B. Slemmons, Bull. Seismol. Soc. Am. **86**, 761 (1996).
19. K. M. Hodgkinson, R. S. Stein, G. Marshall, J. Geophys. Res. **101**, 25437 (1996).
20. D. B. Slemmons, A. E. Jones, J. I. Gimlet, Bull. Seismol. Soc. Am. **55**, 537 (1965).
21. D. I. Doser, J. Geophys. Res. **91**, 12572 (1986).
22. D. I. Doser, J. Geophys. Res. **93**, 15001 (1988).
23. R. E. Abbott, J. N. Louis, S. J. Caskey, S. Pullammanappallil, J. Geophys. Res. **106**, 4169 (2001).
24. We define NRMS as $[(d_i - m_i)^2/N]^{1/2}$, where d_i = data, m_i = model, and N = number of data points.
25. R. D. Catchings, Geol. Soc. Am. Bull. **104**, 117 (1992).
26. J. J. Lienkaemper, Bull. Seismol. Soc. Am. **74**, 2357 (1984).
27. F. F. Pollitz, G. Peltzer, R. Burgmann, J. Geophys. Res. **105**, 8035 (2000).
28. G. Kaufmann, F. Amelung, J. Geophys. Res. **105**, 16341 (2000).
29. T. Nishimura, W. Thatcher, J. Geophys. Res. **108**, 2389 (2003).
30. B. G. Bills, D. R. Currey, G. A. Marshall, J. Geophys. Res. **99**, 22059 (1994).
31. J. E. Dixon, T. H. Dixon, D. Bell, R. Malservisi, Earth Planet. Sci. Lett. **222**, 451 (2004).
32. The postseismic model predicts at the latitude of the GPS profile (~39.3°N) a 2-mm extension across the CNSB in a roughly east-west direction. Removing this from the GPS vectors of (7) leaves secular deformation of 0 to 2 mm/year, also roughly oriented east-west. Further north at the latitude of another GPS profile at 41°N latitude (37), the predicted postseismic deformation is less than 1 mm/year.
33. T. H. Dixon, S. Robaudo, J. Lee, M. C. Reheis, Tectonics **14**, 755 (1995).
34. R. Malservisi, T. H. Dixon, P. C. La Femina, K. P. Furlong, Geophys. Res. Lett. **30**, 10.1029/2003GL017408 (2003).
35. A. D. Frankel et al., U.S. Geol. Surv. Open-File Rep. 02-420 (2002).
36. F. Amelung, J. Bell, J. Geophys. Res. **108**, 10.1029/2002JB001953 (2003).
37. W. C. Hammond, W. Thatcher, J. Geophys. Res. **110**, 10.1029/2005JB003678 (2005).
38. We thank J. Bell, T. Dixon, P. LaFemina, G. Sella, and B. Hammond for discussions and comments, and W. Lengert for encouragement. SAR data were provided by the European Space Agency through a Category 1 project and the Western North America Interferometric Synthetic Aperture Radar Consortium (WinSAR). Supported by the National Earthquake Hazard Reduction Program, NASA Solid Earth Natural Hazard, the NSF EarthScope program, and CSTARS contribution number 3.